# Low-Profile Two-Port MIMO Terminal Antenna for Low LTE Bands with Wideband Multimodal Excitation

Hanieh Aliakbari [1] and Buon Kiong Lau [2]

[1]Lund University
[2]Affiliation not available

October 30, 2023

**Abstract**

It is challenging to design multiple-input multiple-output (MIMO) terminal antennas for LTE bands below 1 GHz, due to the conventional chassis offering only one resonant characteristic mode. Recently, it was shown that minor structural changes can yield additional resonant mode(s), which were used to design two-port MIMO antennas. However, the resulting bandwidth for the second port does not cover the low LTE bands. Herein, a new approach to structural changes and feed design is proposed for the design of a low profile (4 mm) two-port MIMO antenna that covers all common low LTE bands (0.75-0.96 GHz) with total efficiency of above 67%. The large symmetric bandwidth (25%) is achieved using three additional resonant modes obtained by structural changes as well as two simple probe-feed ports jointly exciting weighted combinations of the four modes over frequency. The envelope correlation coefficient of below 0.15 is facilitated by the different phase shifts of the characteristic electric fields at the port locations. Moreover, the design requires no ground clearance, no decoupling structure and the two ports are separated by only 0.2 wavelength. Finally, to show design flexibility, a third antenna is added to the top of the chassis to create a three-port MIMO antenna

# Low-Profile Two-Port MIMO Terminal Antenna for Low LTE Bands with Wideband Multimodal Excitation

Hanieh Aliakbari, *Graduate Student Member, IEEE*, and Buon Kiong Lau, *Senior Member, IEEE*

***Abstract*—It is challenging to design multiple-input multiple-output (MIMO) terminal antennas for LTE bands below 1 GHz, due to the conventional chassis offering only one resonant characteristic mode. Recently, it was shown that minor structural changes can yield additional resonant mode(s), which were used to design two-port MIMO antennas. However, the resulting bandwidth for the second port does not cover the low LTE bands. Herein, a new approach to structural changes and feed design is proposed for the design of a low profile (4 mm) two-port MIMO antenna that covers all common low LTE bands (0.75-0.96 GHz) with total efficiency of above 67%. The large symmetric bandwidth (25%) is achieved using three additional resonant modes obtained by structural changes as well as two simple probe-feed ports jointly exciting weighted combinations of the four modes over frequency. The envelope correlation coefficient of below 0.15 is facilitated by the different phase shifts of the characteristic electric fields at the port locations. Moreover, the design requires no ground clearance, no decoupling structure and the two ports are separated by only 0.2 wavelength. Finally, to show design flexibility, a third antenna is added to the top of the chassis to create a three-port MIMO antenna.**

***Index Terms*—MIMO systems, terminal antennas, wideband antennas, complex correlation coefficient, characteristic modes.**

## I. Introduction

MULTIPLE-input multiple-output (MIMO) technology enables data rate to scale linearly with the number of antennas for a fixed transmit power and bandwidth [1]. It is in widespread use in Long Term Evolution (LTE), IEEE 802.11ac and other wireless communication systems [1]. However, implementing more than one antenna per band in user terminals is challenging in mobile communications, especially in frequency bands below 1 GHz, due to their compact form factor [2]. The small electrical size of the terminal chassis offers limited degrees of freedom (in terms of the number of resonant modes) to fulfill strict requirements of orthogonal MIMO antenna and wideband design. Moreover, the current trend points to lesser space for antennas in smartphones, e.g., decreasing thickness and ground clearance.

Manuscript received Mar. 02, 2020. This work was supported by Vetenskapsrådet under Grants No. 2010-00468 and No. 2018-04717.

The authors are with the Department of Electrical and Information Technology, Lund University, 221 00 Lund, Sweden (e-mails: hanieh.aliakbari_abar@eit.lth.se; buon_kiong.lau@eit.lth.se).

Color versions of one or more of the figures in this paper are available online at http://ieeexplore.ieee.org.

Digital Object Identifier

In recent years, many MIMO terminal antennas have been proposed, e.g., [3]-[23]. For the designs involving cellular bands above 1 GHz [3]-[9], low coupling and correlation can be more easily achieved across the antenna ports via space, angle or polarization diversities, due to the electrically larger chassis facilitating more resonant orthogonal radiation modes, i.e., characteristic modes (CMs) [9]. In fact, high-end smart-phones are already equipped with four-port MIMO antennas for higher LTE bands [24].

On the other hand, below 1 GHz, the largest dimension of the terminal chassis is typically less than half-wavelength ($\lambda_0/2$). This results in the chassis having only one resonant mode [10], [11] (often called fundamental dipole mode), which has a large bandwidth. Hence, early designs of two-port MIMO antennas often lead to either a narrowband solution for the second port, by avoiding the use of the wideband single resonant mode [10]-[12], or solutions that mainly excite the single-mode using both ports, which cause high coupling and correlation [17]-[20]. In addition, the profile (thickness) of modern terminals is typically less than 10 mm, which is electrically very small for frequencies below 1 GHz. This requirement often necessitates larger off-ground clearance as a compromise to achieve acceptable bandwidth and MIMO performance.

Because of the fundamental challenges discussed above, MIMO terminal antennas for low LTE bands are so far confined to only two-port designs [10]-[23]. CM analysis (CMA) has been used in [10]-[16] to reduce the correlation of the two ports in the low band. This is motivated by the far-field orthogonality of CMs, which provides an effective framework to design orthogonal MIMO antennas. In [10], it is shown a dual-antenna configuration of a slot-monopole and a planar inverted-F antenna (PIFA) achieves the measured isolation and envelope correlation coefficient (ECC) of 13 dB and 0.04, if the slot monopole placed at a short end is used to excite the fundamental chassis mode, whereas the PIFA is located at the chassis center to avoid exciting the chassis mode. However, without exploiting the chassis for radiation, the 6 dB bandwidth pf the PIFA is as small as 1%, limiting the practical use of this approach. A magnetic antenna at either short end of the chassis can be used to replace the PIFA [11]. But again, since the magnetic antenna's location is chosen to avoid exciting the chassis, the high isolation of over 20 dB and low ECC of below 0.01 are obtained at the expense of small bandwidth (i.e., 2%).

To increase the bandwidth of the second port while retaining high isolation between the two ports, two additional modes were made resonant in the low band by chassis modification [13]. However, since only one of the two modes was utilized to design the second port, the resulting bandwidth is still small (i.e., 9%) and the profile is as large as 8 mm. In [14], both of the two additional modes were tuned and excited for the second port, which slightly increased the bandwidth to 11%, and the profile is unchanged. Moreover, dual-band design was achieved using CMA for the proposed MIMO antenna in [14]. Generally in [13]-[16], using different modes for each port in resulted in lower bandwidth for one of the ports. Whereas asymmetrical bandwidths may be suitable for early releases of LTE, e.g., Release 8 only requires MIMO operation for the downlink, symmetrical bandwidths are also needed in later releases, e.g., Release 10 (LTE-Advanced), to improve the uplink.

To simultaneously increase the bandwidth for the two ports, two conventional inverted-F antennas (IFAs) located at the two smaller sides of the chassis were proposed [21]. The design covers the LTE low bands across both ports, with measured efficiencies of 45-65% and ECC of less than 0.1. However, in this design, the two self-resonant antennas were well separated (i.e., 150 mm or $\lambda_0/2$ at 1 GHz) and they require a ground clearance of 16 mm and a profile of 7 mm. The two low-band ports in [22] were designed for a metal-framed chassis using the same idea of placing the ports far away from each other, and they achieve measured efficiencies of above 47%, isolation of above 10 dB and ECC of below 0.35. They require a ground clearance of 10 mm and the metal frame limits the chassis profile to 7.5 mm. On the contrary, the longer sides of the chassis were utilized for the two IFA-design in [23] and the ground clearance is smaller (i.e., 2 mm). The structure is reconfigurable by on/off switching and the total efficiency is about 50%, but the correlation is quite high (ECC of up to 0.5).

A symmetric bandwidth of 25% was achieved for the two antenna ports in [18] by each exciting a combined current mode. Defined by means of observing current distributions on the chassis, the two combined modes are formed from the monopole antenna elements' self-resonant mode and the chassis' fundamental dipole mode. The self-resonant mode of each monopole requires a ground clearance of 12 mm, and the antenna element itself further extends this length by 7 mm. Even though the ECC is above 0.3 and the total efficiency is relatively low (i.e., above 45%) at the low LTE bands, this work shows that two different modes can be excited jointly at each of the two ports for MIMO operation, which also conveniently result in symmetric bandwidths. In fact, the same principle has been demonstrated using CMA in an earlier work [8] at a higher frequency (e.g., 2.3 GHz), where two modes are simultaneously excited by two MIMO antenna ports. It is shown using modal weighting coefficients that pattern orthogonality between the ports is achieved by means of phase difference in the excitation of one of the two ports. These pioneering designs [8], [18] focus on the analysis of the antenna operation after the feeding ports are chosen, rather than directly applying this principle to design the feeds. Nevertheless, they provide the insight that it is not necessary to excite different characteristic modes in different ports [13], [14]. Moreover, self-resonant antenna structures (e.g., PIFA, monopole and slot antennas), which are bulkier than their non-resonant coupling elements, are typically used for excitation by at least one of the two ports [10]-[15], [18], [19], [21]-[23]. Hence, efforts were made to completely avoid using self-resonant structures in MIMO antennas [9], [25].

In this paper, we propose a compact two-port MIMO antenna design for low LTE bands with low profile, no ground clearance and no extra switch. Based on the addition of shorted strips (T-strips) along the longer sides of the flat chassis as the initial structure modification [13], [14], the profile was reduced to 4 mm by folding the strips. As can be expected, the folding slightly increased the resonant frequency and decreased the modal bandwidth of the strip-induced mode. In addition, the position of the shorting pin along each strip was moved away from the center position to decrease the resonant frequencies and increase the bandwidth potential. Finally, a slot was added to each of the two longer sides of the chassis, just below the strips, to enhance the bandwidth at the high frequency edge. Taking advantage of the four resonant modes that were optimized over the desired frequency range, two probe feeds were designed to replace the shorting pins to capacitively couple power into the relevant modes to achieve wideband performance for both ports and low ECC (below 0.15) over the entire operating band of 0.75-0.96 GHz.

To enable multiple modes to be simultaneously excited by both ports but yet retaining orthogonality, the feed design ensures that the condition for orthogonality in [8] is retained over the entire band of interest. In particular, the chosen feed location excites one mode with the same phase but the other mode in an out-of-phase fashion. To our knowledge, the proposed two-port antenna is the first low profile (4 mm), on-ground (i.e., no ground clearance) design that simultaneously facilitates low correlation (without decoupling structure), wide bandwidth and high total efficiency over the low LTE band.

To highlight another advantage of the design, which does not occupy either the top or bottom part of the chassis normally reserved for conventional antennas, a third port is added to the top end to create a low-band three-port MIMO antenna, for the first time. The third port consists of a frequency tunable narrow-band antenna [11], which has little effect on the existing ports.

It should be noted that some preliminary results of this work reported in [26] show that the simulated low band bandwidth is only 11% (0.85-0.95 GHz), with isolation of over 15 dB. The relatively poor performance is due to the new resonant mode introduced by the slots in the chassis not being properly utilized by this early design to enhance bandwidth.

## II. MIMO Analysis using Characteristic Mode Theory

In this section, CMA is briefly revisited, in the context of MIMO antenna design and analysis. CMs are real current modes that can be computed numerically for conducting bodies of arbitrary shape. To obtain these modes, the weighted eigenvalue equation should be solved [27]

$$X\,\mathbf{J}_n = \lambda_n R\,\mathbf{J}_n\,, \tag{1}$$

where $\mathbf{J}_n$ is the $n$th characteristic current associated with the $n$th eigenvalue $\lambda_n$. $R$ and $X$ are the real and imaginary parts of the symmetric impedance operator $Z$. Specifically, the CM far-fields produced by $\mathbf{J}_n$ are orthogonal to each other [27]. Thus, for the electric farfield $\mathbf{E}_n$

$$\frac{1}{2Z_0}\left\langle \mathbf{E}_m, \mathbf{E}_n^* \right\rangle = \delta_{mn} = \begin{cases} 1, & m = n \\ 0, & m \neq n \end{cases}, \tag{2}$$

where $\delta_{mn}$ is the Kronecker delta and $Z_0$ is the wave impedance of free space and $^*$ denotes complex conjugate opepration. Also, the symmetric product of the two vector functions in (2), for $\mathbf{A}$ and $\mathbf{B}$ on the surface at infinity $S_\infty$ (i.e., far-field) is defined as

$$\left\langle \mathbf{A}, \mathbf{B} \right\rangle = \oiint_{S_\infty} \mathbf{A}.\mathbf{B}^* ds \,. \tag{3}$$

The orthogonality feature of CM far-fields is ideally suited for MIMO antenna design and analysis. This is because MIMO systems (e.g., LTE) are typically used in rich multipath environments, where the angular power spectrum of the outgoing or incoming signal is nearly uniform. In such a propagation environment, orthogonal patterns of MIMO antenna elements are sufficient to guarantee uncorrelated signals across the antenna ports [2]. Therefore, as long as each antenna port excites one or more than one unique modes, with no mode being excited by more than one port, all the resulting patterns will be pairwise uncorrelated, as illustrated by (2), and likewise the received signals at antenna ports will be pairwise uncorrelated.

However, selective excitation of resonant CMs is sufficient, but not necessary to guarantee orthogonal antenna ports, as explained in the following. Consider a $P$-port MIMO antenna ($P$ = 2 in this work), $\mathbf{E}^p$ is denoted as the excited electric field (E-field), when the $p$th port is excited by an impressed E-field $\mathbf{E}_i^p$. Since CM far-fields form a set of orthogonal functions, they can be used to expand the excited field $\mathbf{E}^p$ [27]

$$\mathbf{E}^p = \sum_{n=1}^{\infty} \alpha_{n,p} \mathbf{E}_n \simeq \sum_{n=1}^{N} \alpha_{n,p} \mathbf{E}_n \tag{4}$$

where $N$ is the number of dominating modes (with small absolute values of $\lambda_n$) and $\alpha_{n,p} = \left\langle \mathbf{J}_n, \mathbf{E}_i^p \right\rangle \big/ (1 + j\lambda_n)$ denotes the modal weighting coefficient of the $n$th CM for the $p$th port.

To evaluate the magnitude and phase of the contribution of the $n$th CM to the far-field radiation pattern of the $p$th port, the complex correlation coefficient (CCC) between $\mathbf{E}^p$ and $\mathbf{E}_n$ is given by [28]

$$\rho_{n,p} = \alpha_{n,p} \big/ \sqrt{P_{rad}} \,, \tag{5}$$

where $P_{rad}$ is the constant total radiated power at each port, and the power budget implies that

$$\sum_{n=1}^{N} \left|\rho_{n,p}\right|^2 \simeq 1 \,. \tag{6}$$

Using (4), if $P$ = 2 and $N$ = 2, the E-fields for the ports are

$$\begin{aligned} \mathbf{E}^1 &= \alpha_{1,1}\mathbf{E}_1 + \alpha_{2,1}\mathbf{E}_2 \\ \mathbf{E}^2 &= \alpha_{1,2}\mathbf{E}_1 + \alpha_{2,2}\mathbf{E}_2 \end{aligned}, \tag{7}$$

The CCC of the far-field patterns for ports becomes

$$\begin{aligned} \rho_{\mathbf{E}^1,\mathbf{E}^2} &= \frac{\left\langle \mathbf{E}^1, \mathbf{E}^2 \right\rangle}{\sqrt{\left\langle \mathbf{E}^1, \mathbf{E}^1 \right\rangle \left\langle \mathbf{E}^2, \mathbf{E}^2 \right\rangle}} = \frac{\alpha_{1,1}\alpha_{1,2}^* + \alpha_{2,1}\alpha_{2,2}^*}{\sqrt{\left|\alpha_{1,1}\right|^2 + \left|\alpha_{2,1}\right|^2}\sqrt{\left|\alpha_{1,2}\right|^2 + \left|\alpha_{2,2}\right|^2}} \\ &= \rho_{1,1}\rho_{1,2}^* + \rho_{2,1}\rho_{2,2}^* \,. \end{aligned} \tag{8}$$

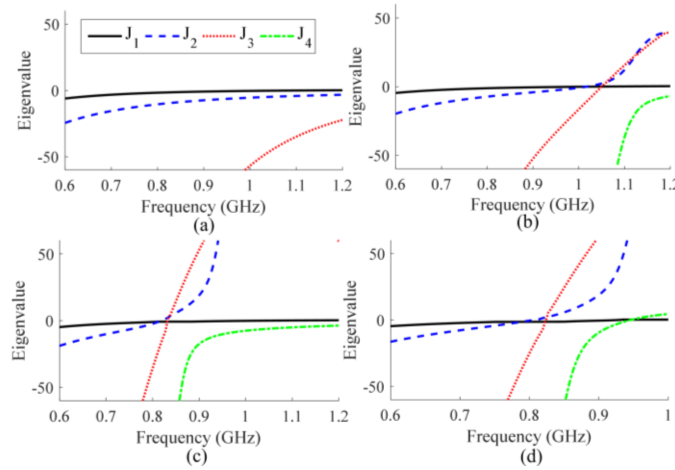


Fig. 1. Eigenvalues of four CMs of interest for the: (a) chassis, (b) chassis with folded strips and center shorting pins, (c) chassis with folded strip and offset shorting pins on the same side, (d) slotted chassis with folded strip and offset shorting pins in same side. Only modes relevant to the design are shown.

Therefore, as noted in [8] in the equivalent context of modal currents, the individual terms $\alpha_{1,1}\alpha_{1,2}^*$ and $\alpha_{2,1}\alpha_{2,2}^*$ do not need to be zero for the sum to be zero, i.e., the general case when ports 1 and 2 do not excite different modes. For example, if ports 1 and 2 excite modes 1 and 2 by the same magnitude ($\left|\alpha_{1,1}\right| = \left|\alpha_{2,1}\right| = \left|\alpha_{1,2}\right| = \left|\alpha_{2,2}\right|$), but in a co-phase manner at port 1 ($\angle\alpha_{1,1} = \angle\alpha_{1,2}$) and 180° out-of-phase at port 2 ($\angle\alpha_{2,1} = \angle\alpha_{2,2} + \pi$), then $\rho_{\mathbf{E}^1,\mathbf{E}^2} = 0$ despite nonzero individual terms.

Another important point in CMA is that the tracking of eigenvalues obtained from (1) over a wide frequency band is very challenging, especially when new modes are introduced by chassis modification [13]- [15], [25]. The orthogonality of far-field patterns in (2) at a given frequency is also a suitable property to be used for modal tracking [29]. The eigenvalues of four CMs of interest in this work (see Fig. 1) were classified by the far-field tracking method of [29], which correlates the far-field patterns of each individual mode over frequency. The method was also applied for MIMO antenna design [14]. In contrast, in the preliminary study [26], a current-based tracking method [25] was used, and it failed to identify and track one of the modes, resulting in the missing mode ($\mathbf{J}_4$) not being used to enhance bandwidth.

## III. CM Modification and Excitation

In Fig. 1, the evolutions of the CMs of interest with minor chassis modifications for the entire design procedure are summarized in eigenvalue plots. The size of the terminal chassis was chosen to be 130 mm × 60 mm, to represent a typical case (e.g., the overall outer dimensions of Samsung S9 is 147.7 mm × 68.7 mm × 8.5 mm). As the first design step, the characteristic eigenvalues for the 130 mm × 60 mm perfect electric conductor (PEC) chassis were computed and shown in Fig. 1(a). As can be seen, the chassis supports only one resonant mode ($\mathbf{J}_1$) close to 1 GHz. Two non-resonant modes of interest to this study ($\mathbf{J}_2$ and $\mathbf{J}_3$) are also shown in Fig. 1(a). In Fig. 2, the currents and the corresponding electric far-field patterns of $\mathbf{J}_1$ to $\mathbf{J}_3$ are shown as a reference. It can be seen that mode 1 ($\mathbf{J}_1$)

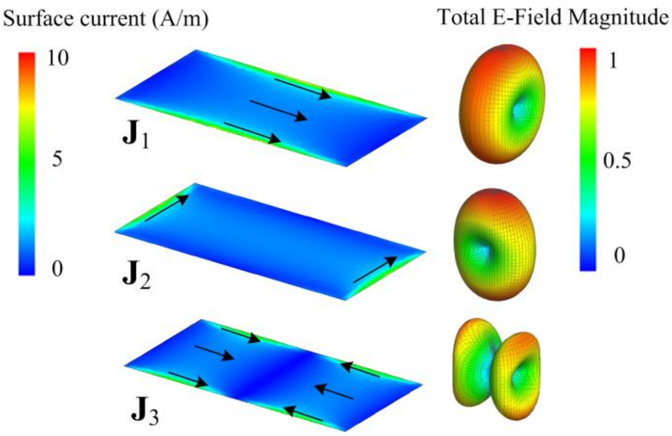


Fig. 2. Eigencurrent distribution and normalized pattern of CMs in the chassis with resonant frequencies of: 1.08 GHz (**J**$_1$), 2.85 GHz (**J**$_2$), 2.5 GHz (**J**$_3$).

is the fundamental dipole mode, with a current flowing along the length of the chassis. Mode 2 (**J**$_2$) supports a current distribution like a dipole oriented along the width of the chassis. Mode 3 (**J**$_3$) is a longitudinal full-wave dipole mode. The plain chassis is then modified in stages to obtain the desired characteristic properties, as will be described in this section. Figures 3(a)-3(c) illustrate the currents and electric far-field patterns of the CMs associated with the eigenvalues in Fig. 1(b)-(d), respectively, for different design stages.

### *A. Folding of T-Strips and Center Feed Positions*

It is known that capacitive loading along the longer sides of the flat chassis using shorted metal strips (T-strips) enables two additional modes to be resonant below 1 GHz [13], [14], apart from the fundamental dipole mode. Specifically, these are the dipole mode along the width of the chassis [13] as well as a mode resulting from the slots formed between the chassis and the shorted metal strips [14]. However, as described earlier, the proposed antennas in [13] and [14] offer only a modest bandwidth (of up to 11%), with asymmetric bandwidths obtained across the two ports. Moreover, they require a profile of 8 mm and the addition of capacitive coupling elements (CCEs) and/or off-ground self-resonant antenna elements. In this work, the chassis structure with T-strips (shorted in the center) in [13] was adopted as the initial design, based on which all of its limitations were addressed in the following step-by-step design procedure.

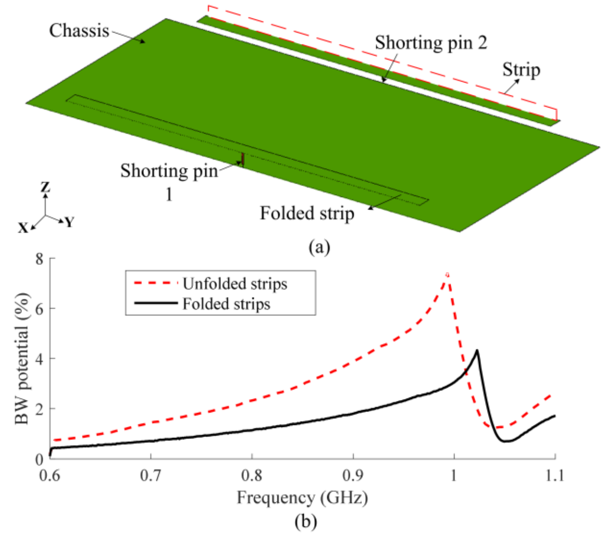


Fig. 4. (a) Chassis layout with unfolded (dashed outline)/folded (solid outline) strips at the two longer sides and with center shorting pins, (b) bandwidth potential of center excited probe feed with unfolded/folded strips.

The first step was to lower the profile of the chassis structure by folding the T-strips into horizontal orientations, as shown in Fig. 4(a). This lowered the overall profile to 4 mm. The resulting eigenvalues, depicted in Fig. 1(b), reveal that the three resonant modes under 1 GHz (see Fig. 2(b) in [13]) are still available, despite the folding. However, by folding the strips, the resonant frequency of **J**$_2$ approaches that of **J**$_3$, and the maximum bandwidth potential [30] of the folded structure (with

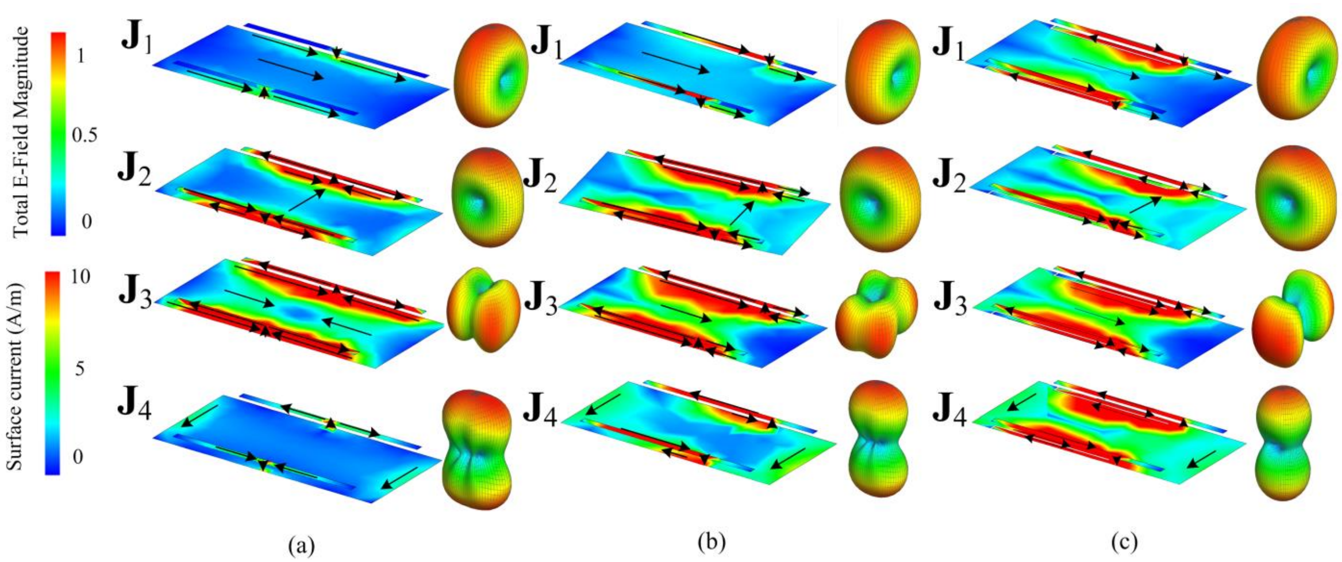


Fig. 3. Eigencurrent distribution and normalized pattern of CMs of chassis with folded strips and (a) center shorting pins with resonant frequencies of: 1.08 GHz (**J**$_1$), 1.01 GHz (**J**$_2$), 1.05 GHz (**J**$_3$), 2.8 GHz (**J**$_4$), (b) offset shorting pins in the same side with resonant frequencies of 1.08 GHz (**J**$_1$), 0.8 GHz (**J**$_2$), 0.83 GHz (**J**$_3$), 1.84 GHz (**J**$_4$), and (c) offset shorting pins in the same side with extra slot on the chassis with resonant frequencies of 1.02 GHz (**J**$_1$), 0.78 GHz (**J**$_2$), 0.83 GHz (**J**$_3$), 0.94 GHz (**J**$_4$).

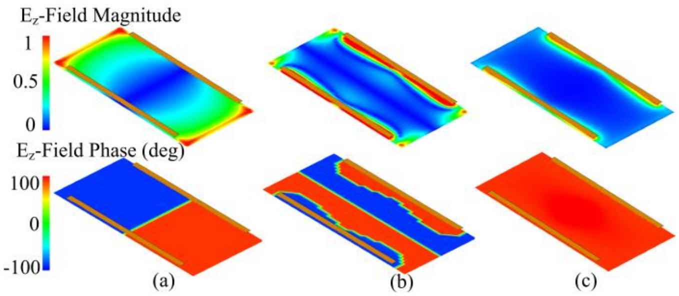


Fig. 5. Magnitude and phase of *z*-directed modal E-field distribution of (a) $\mathbf{J}_1$, (b) $\mathbf{J}_2$, and (c) $\mathbf{J}_3$, 2 mm above the chassis at resonant frequencies.

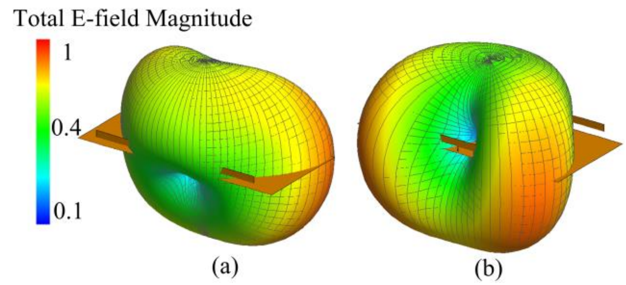


Fig. 6. 3D normalized radiation pattern by exciting individual ports at 1.04 GHz: (b) Port 1; (c) Port 2.

a shorting pin replaced by a probe feed) reduces from 7% to 4.3% (see Fig. 4(b), calculated using BetaMatch) and the frequency of maximum bandwidth potential increases from 0.99 to 1.02 GHz. In addition, as seen in Fig. 1(b), the slopes of $\mathbf{J}_2$ and $\mathbf{J}_3$ are steep (steeper than those of the unfolded case shown in Fig. 2(b) of [13]), whereas that of $\mathbf{J}_1$ is unchanged with the folding. Moreover, $\mathbf{J}_4$ has large eigenvalues below 1 GHz.

Figure 3(a) shows the corresponding eigencurrents and far-field patterns for the chassis with folded strips and centered shorting pins. $\mathbf{J}_1$ has strong currents along the two longer sides of the chassis, giving the classic half-wave dipole pattern along the chassis length. This verifies that the $\mathbf{J}_1$ is the fundamental dipole mode of the chassis. $\mathbf{J}_2$ has strong currents flowing along the strips and the chassis underneath them, due to the capacitive loading of the strips. However, these currents flow in opposite directions, hence it is the currents along the chassis width that contributes to the dipole pattern. In comparison to $\mathbf{J}_1$ and $\mathbf{J}_4$, the currents in the $\mathbf{J}_2$ and $\mathbf{J}_3$ are stronger around the metal strips and shorting pins. Nonetheless, the far-field patterns of $\mathbf{J}_2$ and $\mathbf{J}_3$ are different, since the currents' directions at two shorting pins are opposite in $\mathbf{J}_2$, but the same in $\mathbf{J}_3$. In contrast to $\mathbf{J}_1$, the far-field patterns of $\mathbf{J}_2$ and $\mathbf{J}_4$ are both along the chassis width; however, it is more directional for $\mathbf{J}_4$, since the currents on the strips also contribute to the pattern.

Figure 5 shows the magnitude and phase of the *z* component of the E-field 2 mm above the chassis for the first three modes (i.e., $\mathbf{J}_1$-$\mathbf{J}_3$). As shown in Fig. 5(b), it is expected that if the shorting pins in the center of the chassis are replaced by two (*z*-oriented) feeding ports (unmatched, unless otherwise stated), the electric near-field excitation of $\mathbf{J}_2$ by ports 1 and 2 will be 180° out-of-phase. In contrast, as shown in Fig. 5(c), $\mathbf{J}_3$ is excited by the two ports without any phase shift. Moreover, as the fundamental mode ($\mathbf{J}_1$) has a lower E-field magnitude at the ports, as compared with those of $\mathbf{J}_2$ and $\mathbf{J}_3$ (see Fig. 5(a)), the contribution of $\mathbf{J}_1$ to the overall radiation should be low. This can be confirmed by computing the magnitude and phase of the CCC using (5) for each port at three different frequencies around the resonances of $\mathbf{J}_2$ and $\mathbf{J}_3$ (see Table I). The percentage power in each mode for a given port is given by the magnitude square of the CCC. i.e., $|\rho_{p,n}|^2$. From Table I, it is computed that 99% of total radiation power in each port is radiated by $\mathbf{J}_2$ and $\mathbf{J}_3$, with little contribution from $\mathbf{J}_1$. As expected from Fig. 5(b), it is confirmed in Table I that the excitation of $\mathbf{J}_2$ by ports 1 and 2 are 180° out-of-phase and $\mathbf{J}_3$ is excited in-phase.

TABLE I
CCC BETWEEN EMBEDDED RADIATION PATTERNS AND CHARACTERISTIC FAR-FIELD PATTERNS IN FIG. 3(A).

| | **Mode 1** | **Mode 2** | **Mode 3** |
|---|---|---|---|
| **@1.02 GHz** | | | |
| Port 1 | 0.05∠0° | 0.97∠-16.4° | 0.24∠-96° |
| Port 2 | 0.05∠180° | 0.97∠163° | 0.24∠-96° |
| **@1.04 GHz** | | | |
| Port 1 | 0.01∠-4.6° | 0.72∠-55.3° | 0.69∠73.8° |
| Port 2 | 0.01∠178° | 0.72∠123.2° | 0.69∠73.8° |
| **@1.05 GHz** | | | |
| Port 1 | 0.02∠-11° | 0.3∠39° | 0.95∠-65.8° |
| Port 2 | 0.02∠168° | 0.3∠-148° | 0.95∠-65° |

Due to the lower eigenvalue of $\mathbf{J}_2$ at 1.02 GHz, it has more contribution to the far-field patterns than $\mathbf{J}_3$. Hence, the total patterns of both ports are similar to the pattern of $\mathbf{J}_2$, indicating high correlation. However, at 1.04 GHz, the far-field patterns are almost equally contributed by $\mathbf{J}_2$ and $\mathbf{J}_3$, with 180° phase difference in the excitation of $\mathbf{J}_2$ by the two ports. Thus, the CCC of the two ports is nearly zero at 1.04 GHz. The pattern orthogonality can be visualized by significant differences in the far-field patterns of the two unmatched ports (see Fig. 6). However, as the frequency increases further to 1.05 GHz, the patterns of two ports are dominated by $\mathbf{J}_3$, degrading the pattern orthogonality of the two ports. Therefore, it is concluded that pattern orthogonality is only achieved for a small bandwidth. Moreover, as mentioned, Fig. 4(a) shows that the maximum bandwidth that can be achieved for the folded strips' case with the center-feed ports is also small 4.3%. To match both ports at the frequency of maximum bandwidth potential (1.02 GHz, see Fig. 4(a)), a two Murata element matching network consisting of a parallel inductor ($L$ = 2 nH) and a series capacitor ($C$ = 12 pF) was used at each port.

Although the folding the strips has resulted in a smaller bandwidth (from 7% to 4.3%) and poor ECC performance, the performance limitation is mostly due to the two center-feed ports not exciting the wideband $\mathbf{J}_1$ mode. Therefore, to enlarge the bandwidth, $\mathbf{J}_1$ should also be excited by two ports.

### B. *Offset Feed Positions*

To utilize $\mathbf{J}_1$, it is necessary to offset the two feeding ports (probe feeds) from the center of the strips, so to excite its electric near-field (see magnitude distribution of Fig. 5(a)). Based on this consideration, there are two options, i.e., offsetting the two ports from the center position in the same or the opposite directions along the longer sides. However, from the phase response of Fig. 5(a), it can be seen that these two cases differ in that the same-direction offset results in in-phase excitation of $\mathbf{J}_1$, whereas the opposite-direction offset result in 180° out-of-phase excitation. On the other hand, both offset cases result in equal magnitude but 180° out-of-phase excitation of $\mathbf{J}_2$ (see Fig. 5(b)). Therefore, according to (8) as well as the discussions in Section II, the same-direction offset should provide low correlation between the two ports, whereas the opposite-direction offset should result in high correlation. These predictions are verified in Fig. 7(b), where the ECC exceeds 0.4 for the opposite-direction case but lower than 0.1 for the same-direction offset, within their respective 6 dB impedance bandwidth. As before, both ports in the same-direction offset case were matched at the frequencies of maximum bandwidth (0.8 GHz) with two Murata element matching networks. The parallel inductor value and the series capacitor value were 3.4 nH and 11.4 pF, respectively. Relative to the center fed chassis, the maximum bandwidth potential with the same-direction offset feed increases from 4.3% to 7%, due to the excitation of $\mathbf{J}_1$. Also, as shown in Fig. 7(b), the isolation is larger than 9 dB in the bandwidth (0.77-0.83 GHz).

For further validation of the same-direction offset case, the CCC between each mode and each port was calculated using (5) and summarized in Table II at three frequencies within the 6 dB impedance bandwidth. Similar to the previous case in Table I, it can be observed that $\mathbf{J}_2$ is excited with 180° phase shift and $\mathbf{J}_3$ is excited in phase between the ports. However, contrary to the center-feed chassis, the contribution of $\mathbf{J}_1$ is higher, and it is excited in-phase by the two ports (as expected from Fig. 5(a)). Moreover, the excitation of $\mathbf{J}_3$ is less than that of $\mathbf{J}_1$ and $\mathbf{J}_2$ in the band because of $\mathbf{J}_3$'s narrower bandwidth (compare Figs. 1(b) and 1(c)). Therefore, the total patterns (see Fig. 8) is a combination of the far-field dipole patterns of $\mathbf{J}_1$ and $\mathbf{J}_2$, with a rotation of $\phi \approx 45°$ relative to either modal pattern.

Furthermore, it is shown in Fig. 3(b) that by moving the shorting pins from the center, $\mathbf{J}_1$ has more surface currents around the metal strips and shorting pins (than that in Fig. 3(a)). Compared to the center shorting pins, due to the longer slots formed between the metal strips and the chassis, the resonance frequency of the $\mathbf{J}_2$ and $\mathbf{J}_3$ will shift to lower frequencies and resonance of the $\mathbf{J}_1$ remains almost unchanged (see Fig. 1(c)). The resonant frequency of $\mathbf{J}_4$ is also reduced but it is still far those of the other three modes (i.e., $\mathbf{J}_1$, $\mathbf{J}_2$ and $\mathbf{J}_3$ resonate under 1 GHz). However, in comparison to Fig. 1(b), the slope of $\mathbf{J}_3$ is larger in Fig. 1(c), thus its modal bandwidth is smaller. The resonant frequency of $\mathbf{J}_2$ and $\mathbf{J}_3$ can be tuned with the longer slots (i.e., $L_2$ in Fig. 10) on both sides.

Despite the good ECC performance of the same-direction offset feed structure shown in Fig. 7(b), the bandwidth of 7% (see Fig. 7(a)) is still small and cannot cover the low LTE bands. The isolation performance is likewise only moderate (above 9 dB). Furthermore, even though the impedance bandwidth can be increased using more complex matching networks in BetaMatch (10% bandwidth was achieved with four matching elements), the ECC will increase towards the lower frequencies (e.g., 0.75 GHz) and higher frequencies (e.g., 0.96 GHz). This is because the excitation of $\mathbf{J}_2$ will decrease in those frequencies

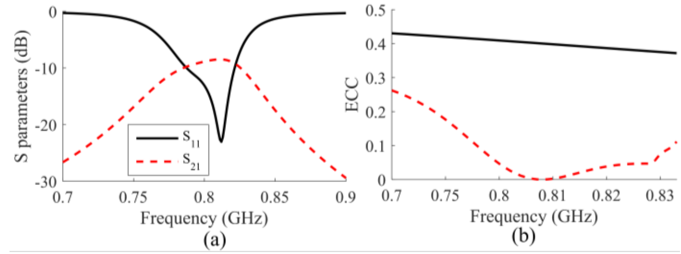


Fig. 7. (a) S parameters of the two matched ports for the offset feed in the same direction and (a) ECC of two matched ports in the operating bandwidth for offset feed in opposite direction (solid) and same direction (dashed).

TABLE II
CCC BETWEEN EMBEDDED RADIATION PATTERNS AND CHARACTERISTIC FAR-FIELD PATTERNS OF FIG. 3(B).

| | **Mode 1** | **Mode 2** | **Mode 3** |
|---|---|---|---|
| **@0.79 GHz** | | | |
| Port 1 | 0.68∠43.6° | 0.72∠36° | 0.16∠-92° |
| Port 2 | 0.68∠43° | 0.72∠-137° | 0.16∠-92° |
| **@0.82 GHz** | | | |
| Port 1 | 0.70∠25.9° | 0.68∠-31.6° | 0.2∠51.4° |
| Port 2 | 0.70∠24° | 0.68∠140° | 0.2∠51.4° |
| **@0.83 GHz** | | | |
| Port 1 | 0.61∠26.1° | 0.66∠118° | 0.43∠79.3° |
| Port 2 | 0.61∠25° | 0.66∠-75° | 0.43∠79.3° |

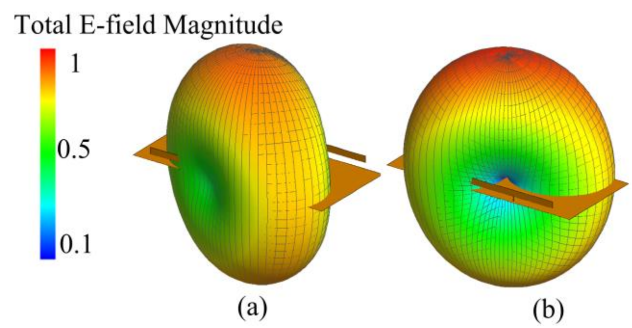


Fig. 8. 3D normalized radiation pattern by exciting individual ports at 0.83 GHz: (a) port 1; (b) port 2.

and $\mathbf{J}_1$ is the only mode which will be excited by the two ports.

### *C. Slotted Chassis*

To increase the bandwidth of both ports at the higher frequency edge, while retaining low ECC, another mode needs to be jointly excited alongside with $\mathbf{J}_1$, to replace the role of $\mathbf{J}_2$ at lower frequencies. Since the E-fields of $\mathbf{J}_1$ excited by the two offset feeds are of equal magnitude and phase (with the feed positions chosen for proper excitation of $\mathbf{J}_1$ and $\mathbf{J}_2$), the two feeds should excite the E-fields of the new mode with equal magnitude and 180° out-of-phase at the two feeds (as was the case for $\mathbf{J}_2$) to ensure that ECC is low, as predicted by (8). As shown in Fig. 1(c), $\mathbf{J}_4$'s resonant is above 1 GHz, so by nature it cannot be used to extend the bandwidth and $\mathbf{J}_2$ has lower modal significance in higher frequencies. However, the E-field distribution of $\mathbf{J}_4$ has the desired property of being equal in magnitude but 180° out-of-phase at the feed locations, as depicted in Fig. 9.

Therefore, the structure should be modified to allow $\mathbf{J}_4$ to contribute to the radiation in the higher frequencies, alongside with $\mathbf{J}_1$. To this end, by inspecting the current distribution of $\mathbf{J}_4$

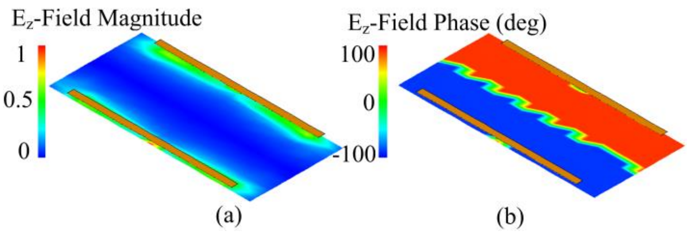


Fig. 9. Magnitude and phase of *z*-directed modal E-field of (a) $\mathbf{J}_1$, (b) $\mathbf{J}_2$, and (c) $\mathbf{J}_3$, 2 mm above the chassis at resonant frequencies.

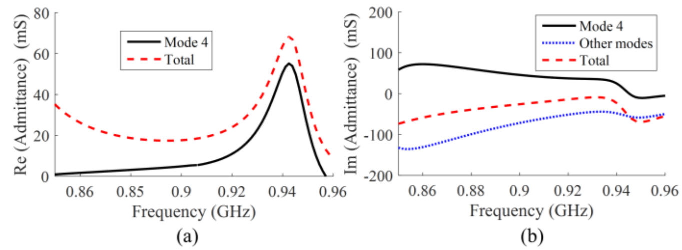


Fig. 11. (a) Real part and (b) Imaginary part of the modal and total admittance.

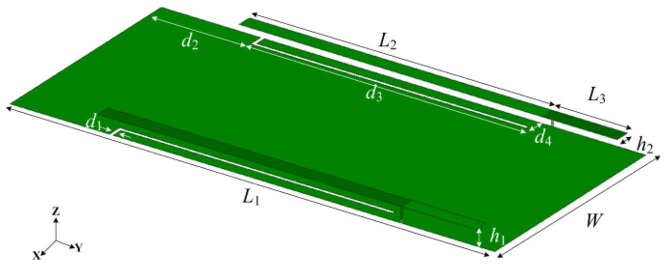


Fig. 10. Final simulated prototype with the total dimensions of 130 × 60 × 4 mm$^3$. The design parameters are: $L_1 = 130$ mm, $L_2 = 81$ mm, $L_3 = 20$ mm, $h_1 = 4$ mm, $h_2 = 4$ mm, $d_1 = 1$ mm, $d_2 = 27$ mm, $d_3 = 74$ mm, $d_4 = 3$ mm, $W = 60$ mm.

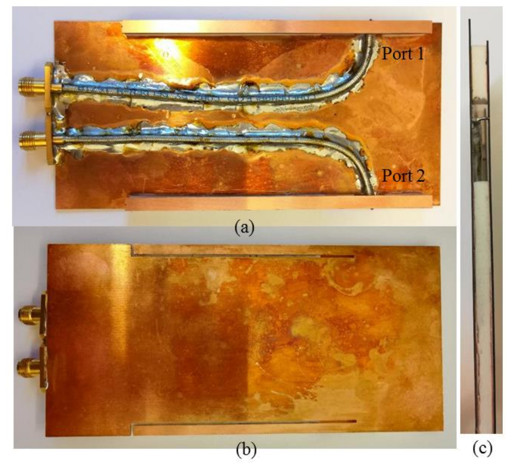


Fig. 12. Fabricated two-port prototype: (a) top, (b) back and (c) side views.

TABLE III
CCC BETWEEN EMBEDDED RADIATION PATTERNS AND CHARACTERISTIC FAR-FIELD PATTERNS OF FIG. 3(C).

| **@0.82 GHz** | **Mode 1** | **Mode 2** | **Mode 3** | **Mode 4** |
|---|---|---|---|---|
| Port 1 | 0.68<5.6◦ | 0.72<-29.4◦ | 0.13<-93.9◦ | 0.1<-90.5◦ |
| Port 2 | 0.69<5.7◦ | 0.69<151◦ | 0.13<-93.9◦ | 0.12<89.5◦ |
| **@0.75 GHz** | | | | |
| Port 1 | 0.65 <-79.9◦ | 0.71<-160◦ | 0.2<-42.5◦ | ~0 |
| Port 2 | 0.65<-79.9◦ | 0.71<16.7◦ | 0.2<-42.5◦ | ~0 |
| **@0.94 GHz** | | | | |
| Port 1 | 0.69<-12.7◦ | ~0 | 0.28<-89◦ | 0.69<62.8◦ |
| Port 2 | 0.67<-15.6◦ | ~0 | 0.22<-89◦ | 0.70<-120◦ |

in Fig. 3(b), the resonant frequency of $\mathbf{J}_4$ can be decreased to below 1 GHz (i.e., 0.94 GHz) by inserting two slots along the longer sides of the chassis, as shown in Fig. 10. In this way, the current path along the chassis width is increased. Similarly, the resonant frequency of $\mathbf{J}_2$ is also decreased to 0.78 GHz, which can contribute to the radiation and improve the ECC at lower frequencies. By the length of this slot (i.e. $d_3$ in Fig. 10), the resonant frequency of $\mathbf{J}_4$ can be tuned. The computed CCC between each mode and each port is shown in Table III for three frequencies. As can be seen, $\mathbf{J}_4$ offers almost equal contribution as $\mathbf{J}_1$ in magnitude, but nearly 180° out-of-phase excitation as compared to $\mathbf{J}_1$'s nearly co-phase excitation. Furthermore, by adding the slot, the frequency of maximum bandwidth potential increases to 0.9 GHz, and the bandwidth potential improves because of one more resonant mode: $\mathbf{J}_4$ adds some reactive admittance (see Fig. 11(b)) to the other modes' reactive admittances and also increases the real part of input admittance at the higher frequencies (see Fig. 11(a)).

Finally, both ports were matched using the BetaMatch software. To match the ports, a three element ∏ matching network consisting of a 4.3 nH series Murata inductor together with 18 pF and 10 pF parallel Murata capacitors was used. One more matching element was used here than the previous cases (in section III. *A* and section III. *B*), as it was needed to improve the matching at the lower frequencies.

## IV. PROTOTYPE VERIFICATION

The proposed antenna was fabricated, as shown in Fig. 12. A copper plate (thickness of 0.5 mm) was used as the chassis of the prototype and Rohacell foams were used to keep the feeding structures at the two longer sides more stable. The foams are electrically neutral ($\varepsilon_r = 1$), so it does not load the modes and change the simulated results. The simulated and measured S parameters given in Fig. 13(a) show good agreement. The final design provides the 6 dB impedance bandwidths of 0.75-0.96 GHz (25%). The measured far-field patterns, shown in Fig. 14, illustrate that a high level of orthogonality is achieved between the two ports at three sample frequencies. The measured ECC is below 0.15 (see Fig. 13(b)) and the measured total efficiency is above 67% (average of 71%) over the impedance bandwidth.

## V. FEASIBILITY OF THREE-PORT ANTENNA AT LOW FREQUENCY BAND

As mentioned earlier, one advantage of the proposed two-port antenna is that it does not need to occupy the top or bottom end of the chassis, typically used for self-resonant antenna elements. Moreover, because of the chassis' electrically small dimensions, achieving more than two uncorrelated ports in the low frequency band is challenging. To our knowledge, no such three-port antenna has been reported.

In this section, extending the proposed two-port wideband design, the feasibility of a three-port structure for low band coverage is studied. In particular, the planar-coupled feed loop

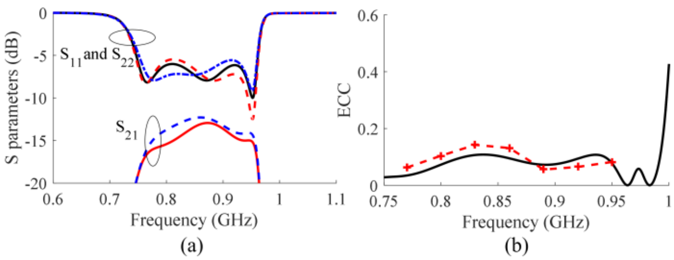


Fig. 13. (a) S parameters and (b) ECC of the simulated (solid lines) and measured (dashed lines) prototype of two-port antenna designed using CMA.

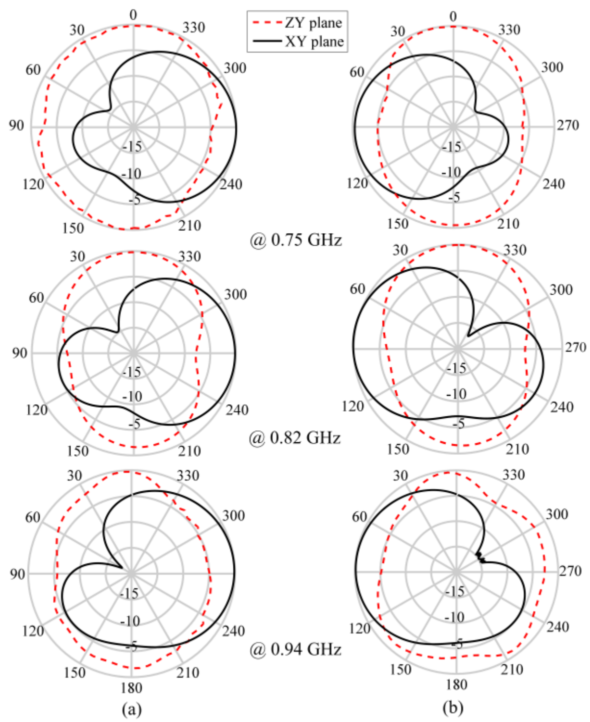


Fig. 14. Measured total radiation patterns of the two-port prototype at three frequencies: (a) port 1 excitation. (b) port 2 excitation.

in [31] was employed to realize the self-resonant magnetic antenna as the third port. The loop antenna [31] was previously adopted in [11] to provide an uncorrelated but narrowband second port for a traditional chassis top/bottom antenna. The antenna occupies 15 mm × 60 mm at the top end of the two-port structure (see Fig. 15), with the total chassis length (130 mm) unchanged. As observed in Fig. 15, the coupled feed loop is implemented on a substrate and consists of two half-square rings, with the inner ring acting as the matching feed and the outer ring as the main radiator [31]. Although the coupled loop makes use of the shorter edge of the chassis, the resonant modes of the chassis is not excited over the existing two ports' 6 dB bandwidth (i.e., magnetic fields of $\mathbf{J}_1$-$\mathbf{J}_4$ are weak at this location). Therefore, only the loop is excited (as a self-resonant structure) and the current is mostly confined around the outer loop (see Fig. 16). Only small amounts of currents are coupled to the slots on the chassis. The parameters of the coupled loop antenna are shown in Fig. 16. It is noted that the operation of the ports 1 and 2 will not be affected by adding the third port so the parameters of the chassis is the same as Fig. 10 and no re-optimization is needed.

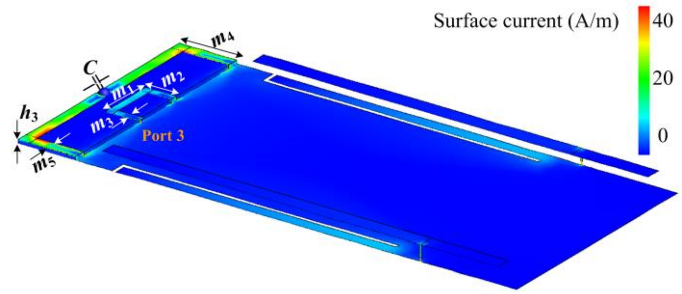


Fig. 15. Current distribution of the 3-port antenna at 0.95 GHz when the loop antenna is excited. The parameters of the loop antenna are: $m_1$ = 15 mm, $m_2$ = 10 mm, $m_3$ = 2 mm, $m_4$ = 15 mm, $m_5$ = 3 mm, $h_3$ = 0.8 mm, $C$ = 0.17 pF. The substrate has a permittivity of 2.45, a loss tangent of 0.003 and a thickness $h_2$.

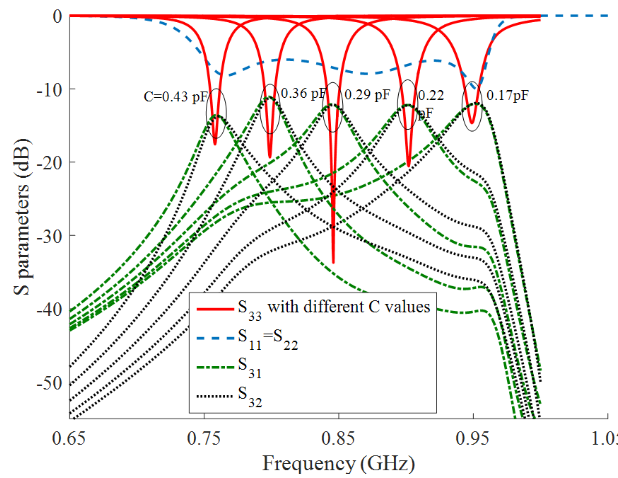


Fig. 16. Simulated S parameters of the coupled loop, with different values of $C$.

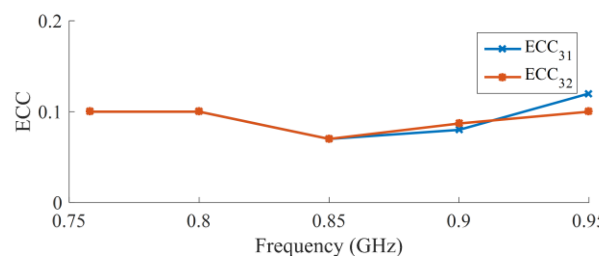


Fig. 17. Simulated ECC of the three port antenna based on far-field patterns.

A major drawback of the coupled loop antenna is the narrow bandwidth [11], [31]. However, it can still be used as a diversity antenna, where a relatively small instantaneous bandwidth is needed (e.g., up to 20 MHz for LTE). To provide coverage over the entire low band, the resonant frequency of the coupled loop antenna (or third port) can be tuned by replacing the fixed capacitor between the two-arm separations of the outer loop (i.e., $C$ in Fig. 15) with a varactor [11]. The S parameters with different capacitance values are shown in Fig. 16. The required tuning range of the varactor is between 0.17-0.43 pF to cover the bandwidth of the other two ports shown in Fig. 13(a). No matching network is needed. The achieved isolation is above 12 dB, which is enough for frequency bands below 1 GHz. More importantly, the ECC between the third port and any of the other ports is below 0.11 for all varactor states (see Fig. 17). The total simulated efficiency of port 3 is above 83% for all the different $C$ values.

## VI. CONCLUSION

This paper presents a concept design of MIMO terminal antennas that relies on the joint excitation of multiple modes with proper phase shifts to drastically improve the impedance bandwidth in the low band while retaining low correlation. To this end, the characteristic currents as well as the amplitude and phase of the electric near-fields of the modes were used to guide the stepwise modifications of a previous strip-loaded chassis. The proposed low-profile two-port design, utilizing direct probe feeds at the loading strips and two added slots on the chassis, achieves the same bandwidth over both ports, covering 0.75-0.96 GHz (25% bandwidth). In addition, it is shown that a narrowband but tunable third antenna port can be added to the unused space typically occupied by traditional self-resonant antenna elements, to provide a three-port MIMO antenna.

## ACKNOWLEDGMENT

The authors would like to thank Andreas Johansson at Lund University for his help in fabricating the antenna prototype.

## REFERENCES

[1] E. Dahlman, S. Parkvall, and J. Sköld, *4G LTE-Advanced Pro and The Road to 5G*, 3rd Ed., Academic Press, 2016.

[2] H. Li and B. K. Lau, "MIMO systems and antennas for terminals," in *Handbook of Antenna Technologies*, Z. N. Chen, Ed. Springer, 2015, pp. 1-35.

[3] M.-Y. Li et al., "Eight-port orthogonally dual-polarized antenna array for 5G smartphone applications," *IEEE Trans. Antennas Propag.*, vol. 64, no. 9, pp. 3820–3830, Sep. 2016.

[4] J. Guo, L. Cui, C. Li, and B. Sun, "Side-edge frame printed eight-port dual-band antenna array for 5G smartphone applications," *IEEE Trans. Antennas Propag.*, vol. 66, no. 12, pp. 7412–7417, Dec. 2018.

[5] Z. Qin, W. Geyi, M. Zhang, and J. Wang, "Printed eight-element MIMO system for compact and thin 5G mobile handset," *Electron. Lett.*, vol. 52, no. 6, pp. 416–418, Mar. 2016.

[6] G. Li et al., "Isolation-improved dual-band MIMO antenna array for LTE/WiMAX mobile terminals," *IEEE Antennas Wireless Propag. Lett.*, vol. 13, pp. 1128–1131, 2014.

[7] M. Ikram, R. Hussain, A. Ghalib, and M. S. Sharawi, "Compact 4-element MIMO antenna with isolation enhancement for 4G LTE terminals," in *Proc. IEEE Int. Symp. Antennas Propag. (APSURSI)*, Fajardo, Puerto Rico, Jun. 2016, pp. 535–536.

[8] K. K. Kishor and S. V. Hum, "A two-port chassis-mode MIMO antenna," *IEEE Antennas Wireless Propag. Lett.*, vol. 12, pp. 690–693, 2013.

[9] R. Martens and D. Manteuffel, "Systematic design method of a mobile multiple antenna system using the theory of characteristic modes*," IET Microw. Antennas Propag.*, vol. 8, no. 12, pp. 887 – 893, 2014.

[10] H. Li, Y. Tan, B. K. Lau, Z. Ying, and S. He, "Characteristic mode based tradeoff analysis of antenna-chassis interactions for multiple antenna terminals," *IEEE Trans. Antennas Propag.*, vol. 60, no. 2, pp.490–502, Feb. 2012.

[11] H. Li, B. K. Lau, Z. Ying, and S. He, "Decoupling of multiple antennas in terminals with chassis excitation using polarization diversity, angle diversity and current control," *IEEE Trans. Antennas Propag*., vol. 60, no. 12, pp. 5947-5957, Dec. 2012.

[12] I. Szini, A. Tatomirescu, and G. F. Pedersen, "On small terminal MIMO antennas, harmonizing characteristic modes with ground plane geometry," *IEEE Trans. Antennas Propag*., vol. 63, no. 4, pp. 1487–1497, Apr. 2015.

[13] H. Li, Z. Miers, and B. K. Lau, "Design of orthogonal MIMO handset antennas based on characteristic mode manipulation at frequency bands below 1 GHz," *IEEE Trans. Antennas Propag*., vol. 62, no. 5, pp. 2756-2766, May 2014.

[14] Z. Miers, H. Li, and B. K. Lau, "Design of bandwidth enhanced and multiband MIMO antennas using characteristic modes," *IEEE Antennas Wireless Propag. Lett*., vol. 12, pp. 1696–1699, 2013.

[15] C. Deng, Z. Feng, and S. V. Hum, "MIMO mobile handset antenna merging characteristic modes for increased bandwidth," *IEEE Trans. Antennas Propag.*, vol. 64, no. 7, pp. 2660–2667, Jul. 2016.

[16] K. K. Kishor, and S. V. Hum, "Multiport multiband chassis-mode antenna design using characteristic modes," *IEEE Antennas and Wireless Propag. Lett.*, vol. 16, pp. 609-612, 2017.

[17] A. A. Al-Hadi and R. Tian, "Impact of multiantenna real estate on diversity and MIMO performance in mobile terminals," *IEEE Antennas Wireless Propag. Lett.*, vol. 12, pp.1712-1715, 2013.

[18] S. Zhang, K. Zhao, Z. Ying, and S. He, "Investigation of diagonal antenna–chassis mode in mobile terminal LTE MIMO antennas for bandwidth enhancement," *IEEE Antennas Propag. Mag.*, vol. 57, no. 2, pp. 217–228, Aug. 2015.

[19] Y. L. Ban, Z. X. Chen, Z. Chen, K. Kang, and J. L. W. Li, "Decoupled closely spaced heptaband antenna array for WWAN/LTE smartphone applications," *IEEE Antennas Wireless Propag. Lett*., vol. 13, pp. 31-34, 2014.

[20] J. Holopainen, J. Ilvonen, R. Valkonen, A. A. H. Azremi, and P. Vainikainen, "Study on the minimum required size of the low-band cellular antenna in variable-sized mobile terminals," in *Proc. 6th Eur. Conf. Antennas Propag., Prague, Czech Republic*, Mar. 26-30, 2012, pp. 2754–2758.

[21] I. Barani, and K. Wong, "Integrated inverted-F and open-slot antennas in the metal-framed smartphone for 2 x 2 LTE LB and 4 x4 LTE M/HB MIMO operations," *IEEE Trans. Antennas Propag.,* vol. 66, no. 10, pp. 5004–5012, Oct. 2018.

[22] D. Huang, Z. Du, and Y. Wang. "A quad-antenna system for 4G/5G/GPS metal frame mobile phones," *IEEE Antennas Wireless Propag. Lett.*, vol. 18, no. 8, pp. 1586-1590, Aug. 2019.

[23] J. Choi, W. Hwang, C. You, B. Jung, and W. Hong, "Four-element reconfigurable coupled loop MIMO antenna featuring LTE full-band operation for metallic-rimmed smartphone," *IEEE Trans. Antennas Propag.,* vol. 67, no. 1, pp. 99–107, Jan. 2019.

[24] Mobile World Live, "Standard configuration for 4.5G smartphones: 4-antenna technology has been deployed on all high-end smartphones and are penetrating medium- and low-end smartphones," 2018. [Online]. Available: https://www.mobileworldlive.com/huawei-updates/standard-configuration-for-4-5g-smartphones-4-antenna-technology-has-been-deployed-on-all-high-end-smartphones-and-are-penetrating-medium-and-low-end-smartphones/ [Accessed: 24 Sep. 2019].

[25] C. Deng, Z. Xu, Aidi Ren, and S. V. Hum, "TCM-based bezel antenna design with small ground clearance for mobile terminals," *IEEE Trans. Antennas Propag*., vol. 67, no. 2, pp. 745-754, Feb. 2019.

[26] H. Li, and B. K. Lau, "Design of low profile MIMO antennas for mobile handset using characteristic mode theory," in *Proc. IEEE 5th Asia-Pacific Conf. Antennas Propag*., Kaohsiung, Taiwan, Jul. 26-29, 2016, pp. 63-64.

[27] R. Harrington and J. Mautz, "Theory of characteristic modes for conducting bodies," *IEEE Trans. Antennas Propag*., vol. AP-19, no. 5, pp. 622–628, Sep. 1971.

[28] E. Safin and D. Manteuffel, "Reconstruction of the characteristic modes on an antenna based on the radiated far field," *IEEE Trans. Antennas Propag.*, vol. 61, no. 6, pp. 2964–2971, Jun., 2013.

[29] Z. Miers and B. K. Lau, "Wide band characteristic mode tracking utilizing far-field patterns," *IEEE Antennas Propag. Lett.*, vol. 14, pp. 1658–1661, 2015.

[30] J. Villanen, J. Ollikainen, O. Kivekäs, and P. Vainikainen, "Coupling element based mobile terminal antenna structures," *IEEE Trans. Antennas Propag*., vol. 54, no. 7, pp. 2142-2153, Jul. 2006

[31] A. Erentok and R. W. Ziolkowski, "Metamaterial-inspired efficient electrically small antennas," *IEEE Trans. Antennas Propag.*, vol. 56, no. 3, pp. 691–707, Mar. 2008.